Environmental Science: Atmospheres

ROYAL SOCIETY OF CHEMISTRY

PAPER

View Article Online
View Journal | View Issue

Cite this: *Environ. Sci.: Atmos.*, 2025, **5**, 378

Ice nucleation onto model nanoplastics in the cirrus cloud regime

Omar Girlanda, [a] Guangyu Li,[ab] Denise M. Mitrano, [a] Christopher H. Dreimol [cd] and Zamin A. Kanji *[a]

The proportion of ice crystals in clouds can affect cloud albedo and lifetime, impacting the Earth's radiative budget. Ice nucleating particles (INPs) lower the energy barrier of ice nucleation and thus facilitate primary ice formation in the atmosphere. Atmospheric nanoplastics (NPs) have been detected in remote regions far from emission sources, suggesting that they can become airborne and undergo long-range transport in the atmosphere. During the atmospheric residence of NPs, they could catalyse primary ice crystal formation by acting as INPs. In this study, we present results from laboratory experiments in which model NPs composed of polystyrene and polyacrylonitrile were tested for their ice-nucleating ability using the horizontal ice nucleation chamber (HINC) as a function of ice-nucleation temperature and water saturation ratio. The results showed that NPs can be effective INPs under both cirrus and cold mixed-phase cloud conditions. The surface characteristics and wettability of the NPs were analysed *via* scanning electron images and dynamic vapour sorption measurements, which revealed the freezing mechanism as a combination of deposition nucleation and pore condensation and freezing. The results highlight the need to enumerate and characterise NPs in the atmosphere, given their potential to get scavenged by clouds *via* primary ice formation in clouds.

Received 24th September 2024
Accepted 4th February 2025

DOI: 10.1039/d4ea00132j

rsc.li/esatmospheres

Environmental significance

Microplastics and nanoplastics are an emerging persistent pollutant of concern. Plastic litter released in aquatic and terrestrial environments is exposed to mechanical abrasion, chemical- and photo-degradation and can fragment into smaller nanoplastic particles which have been detected in remote regions and in cloud water far away from any sources. Here we investigate the atmospheric fate of model polystyrene and polyacrylonitrile nanoplastic particles with respect to ice cloud formation. We find that after ageing in aqueous environments for 10 days, polystyrene particles can have similar ice nucleation abilities to mineral dust illite particles. To assess the true impact of plastics on ice clouds in the atmosphere, constrained estimates of airborne plastic concentrations are needed.

1 Introduction

Primary ice particle formation in the atmosphere can occur homogeneously when a cloud droplet freezes at temperatures below the homogeneous nucleation temperature (HNT, approximately 235 K) under ice supersaturated conditions (relative humidity with respect to ice (RH_i) $\geq$ 140%).[1] At warmer subfreezing temperatures or lower relative humidity, ice formation can also be initiated *via* heterogeneous ice nucleation (IN). IN is catalysed by a subset of aerosol particles called ice nucleating particles (INPs), which lower the energy barrier of the phase transition by providing an interface on which water vapour molecules can deposit or liquid water can aggregate and grow to a supercritical size favouring IN.

Accurate knowledge of INP physicochemical properties and their atmospheric transport is pivotal to understanding ice formation in tropospheric clouds. Depending on the glaciation extent of clouds, their radiative feedbacks[2] and precipitation patterns[3] can differ significantly.[4] Solar radiation that can reach the Earth's surface and surface radiation emitted to space are strongly influenced by the partitioning between liquid droplets and ice crystals in clouds. Cloud phase also influences the Earth's hydrological cycle[5] as the ice phase is responsible for the initiation of the majority of rainfall over mid-latitudes.[3] Known atmospheric particles that are efficient INPs include mineral dust,[6–10] volcanic ashes,[11] biogenic particles,[12,13] marine organics,[14] bacteria,[15] as well as organic matter.[16] It has been demonstrated that anthropogenic pollutants such as soot emitted from combustion engines[17] can also act as INPs in the cirrus cloud regime. Recent studies[18–22] questioned the potential influence of other prevalent pollutants, *e.g.*, plastic particles, on IN.

Plastics are inexpensive materials that are used in many applications. They are designed to be durable, and if not

[a]*Department of Environmental Systems Sciences, ETH Zurich, 8092 Zurich, Switzerland. E-mail: zamin.kanji@env.ethz.ch*

[b]*Laboratory for Microwave Spatial Intelligence and Cloud Platform, Deqing Academy of Satellite Applications, Deqing, China*

[c]*Wood Materials Science, Institute for Building Materials, ETH Zürich, 8093, Zürich, Switzerland*

[d]*Cellulose & Wood Materials Laboratory, Empa, 8600 Dübendorf, Switzerland*

disposed of properly, can enter the environment[23,24] and persist for a long period of time.[25] Plastic litter released in aquatic and terrestrial environments is exposed to mechanical abrasion, chemical- and photo-degradation and can fragment into smaller particles[26–28] to generate microplastics (MP; diameter between 5 mm and 1 μm) and nanoplastics (NP; diameters <1 μm).[29–31] Micro- and nanoplastics (MnP) are also directly emitted to the environment during the use of relevant products such as cleaners and cosmetics.[32,33] As a persistent pollutant, environmental MnP will accumulate and cycle in the Earth's systems for long periods of time.[34]

The sources of airborne plastics can be very diverse[35] and can be best understood as complex (re)suspension and deposition cycles.[18] In urban settings, for example, MnP can be emitted into the atmosphere directly in the wake of vehicles, where turbulence suspends particles produced by the abrasion of tires and brakes.[34,36] MnPs present in agricultural soils[37,38] and landfills[39] can be re-suspended in air by wind erosion.[34,40] In populated areas, MnPs can be directly emitted from processes such as drying laundry[41] and other urban activities.[42,43] In aquatic environments, where MnPs are extensively found,[44–47] the aerosolisation mechanism is similar to the production of aerosol spray emission *via* wave breaking, bubble bursting and jet drop emissions[48,49] or by impact of raindrops.[50] MnPs can then be removed from the atmosphere by dry or wet deposition,[51] and once deposited onto the ground, they could also be exposed to re-suspension and re-enter the atmosphere.[29]

This study focuses on the ability of NPs to act as INPs at high altitudes below 243 K where both ice dominated mixed-phase clouds and ice only clouds can form.[52,53] Although the number of studies that provide evidence of the presence of NPs in the environment is limited, NPs have been measured in remote regions such as the Alps[54] and the Poles.[55] These locations are far from emission sources and suggest that these lightweight particles can be suspended in the atmosphere,[56] reach the free troposphere[57,58] and be transported over long distances before deposition.[22,34,59] The analytical methods typically used to measure environmental MnPs are limited to measure particles >1 μm,[60–62] which consequently may result in an underestimation of NPs concentrations in the atmosphere.[63] Comparisons between MPs and NPs mass concentrations[63] showed that the quantity of MPs and NPs might be similar in atmospheric deposition. Due to their smaller sizes, the number concentration of NPs could therefore be multiple orders of magnitude larger compared to MPs.[63] Recently more work has been done on detecting airborne NPs using aerosol mass spectrometry that identified likely sources of polystyrene NPs from trash incineration.[64]

Aeschlimann *et al.*[18] reviewed aerosol particles known to be good INPs and compared their physiochemical characteristics to MnPs. MnPs are insoluble under atmospheric conditions, providing a solid surface over which freezing could be facilitated. Additionally, ageing and mechanical weathering, either directly in the atmosphere or in water or soil before re-suspension,[65] could induce fractures and cracks on the particle surface and provide active sites[66,67] that favor IN. The surface chemistry of plastics may also influence NPs potential as INPs. The presence of hydrophilic functional groups in some plastics found to be abundant in cloud water[22] favors water adsorption, facilitating IN.[68] However, the IN potential of NPs could also be dependent on other factors such as heteroagglomeration with other aerosols (minerals, clays)[19] or the adsorption of bio-macromolecules[69] and pollutants which alter the surface chemistry.[19] Ganguly and Ariya[19] reported that MnPs can be efficient INPs in the immersion freezing mode depending on several physicochemical characteristics such as morphology, size, surface chemistry, and possible interactions with other atmospheric trace species. A newer study also in the immersion freezing mode, reported that atmospheric ageing can inhibit the IN activity of MPs.[21] Here, we predominantly focus on studies of NPs as INPs in the deposition mode (where water vapor directly deposits and freezes upon contact with the INP, without the presence of liquid water)[9] or *via* the pore condensation and freezing (PCF) mechanism relevant for cirrus cloud formation. PCF[70] occurs when cracks and pores present on the surface of the INP allow water to condense at subsaturated conditions (*via* the inverse Kelvin effect), and subsequently freeze.

In this study, we tested model NPs[71] composed of polystyrene (PS) and polyacrylonitrile (PAN), plastic polymers widely used for packaging and clothing manufacturing. The choice of PS and PAN nanoplastics reflects their prevalence in atmospheric sources, such as urban emissions, and the composition of textile fibers. While actual environmental micro- and nanoplastics encompass a broader spectrum of polymer types and morphologies (*e.g.*, microfibers, microbeads, and weathered fragments), these model particles provide a controlled framework to study fundamental ice nucleation behaviors. Studies such as Wang *et al.*[22] have detected microplastics with varying morphologies and coatings in cloud water, underscoring the importance of investigating how these features influence nucleation activity. The samples were tested for their IN abilities as a function of particle size, morphology, IN temperature and relative humidity. Surface characteristics and water vapor uptake of the tested particles were characterized in order to detect possible active sites and determine the wettability of the particles. The present study does not directly investigate the concept of atmospheric aging on NPs, but shows that storage of synthetic NPs in water suspensions can affect their ability to promote ice formation.

2 Methods

2.1 Model nanoplastics samples

To ensure sufficient quantities of NPs required for IN experiments, model NPs were used. The procedure used to synthesize the particles is described in Mitrano *et al.*[71] Briefly, the emulsion polymerization consists of several steps in which a Pd salt is incorporated into polyacrylonitrile (PAN). From this, PAN NPs are generated and used for the experiment. To produce polystyrene (PS) NPs, an additional step is needed, in which polystyrene is added to the emulsion so that it forms a shell around the particles. The rate of polymer addition at each synthesis step determined the surface morphology of the particles, where it can vary from smooth to bumpy. The final NPs suspension (5% w/w) was monodisperse and stored in a liquid stock solution of water and surfactant (sodium dodecyl sulfate, SDS) to avoid NP

agglomeration. The metal-doping (Pd) of these particles is typically used as a conservative tracer in studies following the fate, transport and biological uptake in various environmental systems, but had no relevance for the IN experiments, as the outer polymer shell ensured that no metal was exposed on the particle surface.[71] The generated particles are negatively charged (about −50 mV) because of the synthesis procedure. However, before the IN experiments commenced, to ensure no aggregates formed during the size selection, they were neutralized and brought to a known Boltzmann distribution of charges using a X-ray neutralizer.

Polymers in the environment often come in a mixture of polymer chemistry, sizes and morphologies which are difficult to separate and have in sufficient quantities.[72] As the chemical composition of our model NPs were already known, they are well-suited for IN experiments and can be considered a proxy for pristine (unweathered without surface coatings of (in)organics) environmental NPs. PS and PAN differ by their chemical composition of the polymer chain. PS ($[C_8H_8]_n$) possesses a pendant phenyl group, which is non-polar, as opposite to PAN ($[C_3H_3N]_n$), which has a polar nitrile bond. For the characterizations and IN experiments, three different batches of PS-NP namely PS1, PS2, PS3 and 2 batches of PAN-NP, PAN1 and PAN2, were tested. Each batch possessed slightly different size distributions and surface morphologies (see 3.1).

2.2 Ice nucleation experiments

Fig. 1 shows a schematic of the experimental setup in two parts. First, the aerosol generation and size selection (1 in Fig. 1) followed by the IN (2 in Fig. 1).

2.2.1 Aerosolisation and size selection. Before particle characterization and further IN experimentation, the stock suspension containing the NPs samples was diluted by 1 : 1000 (volume) using ultra-pure, molecular biology grade water (VWR Chemicals, BHD). This dilutes both the concentration of residual surfactant and the particle concentration present in the solution during the aerosolisation process. We estimate that the residual SDS in the atomized NP suspensions is less than 2×10^{-6} g mL^{-1} based on the initial amount of SDS used (1 g in 500 mL of solution) which is further diluted by a factor of 1000. To generate NPs aerosols from the liquid suspension, the same method as in Kanji and Abbatt (2009)[73] was applied, where a polydisperse aerosol flow was generated by an atomizer, with pure nitrogen (N_2) as a carrier gas. A magnetic stirrer was used to ensure homogeneous mixing of the liquid suspension during the aerosol generation. The NPs aerosol flow was passed through silica-gel and molecular sieve diffusion driers to remove excess moisture. The aerosol flow RH_w was monitored by a RH sensor (ARFTP/R-PT100A/HT-D, Titech GmbH) and kept below 3%. The particles were size selected by their dry electrical mobility equivalent diameter (d_{el}) using a differential mobility analyzer (DMA, Electrostatic Classifier 3082 with a long column 3081 and X-ray radiation source 3087/3088, TSI Inc.). The IN experiments were conducted with NPs particles with a nominal d_{el} = 200 nm. The DMA was operated at a constant sheath flow of 8 L min^{-1}, and the sample flow was 2.5 L min^{-1} to keep the transfer function broad and to transmit enough particles. After the size selection, the monodisperse flow was split by an isokinetic flow splitter (Model 3780, TSI Inc.) and directed to the instruments.

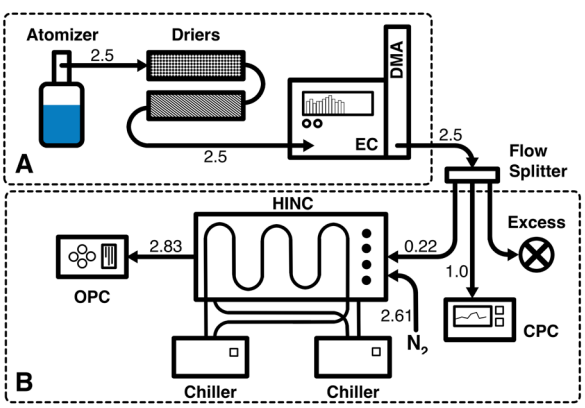

Fig. 1 Schematic of the experimental setup. (A) Aerosolization of the sample and size selection of the NP. (B) Ice nucleation experiment. The numbers indicate the flow rates in L min^{-1}.

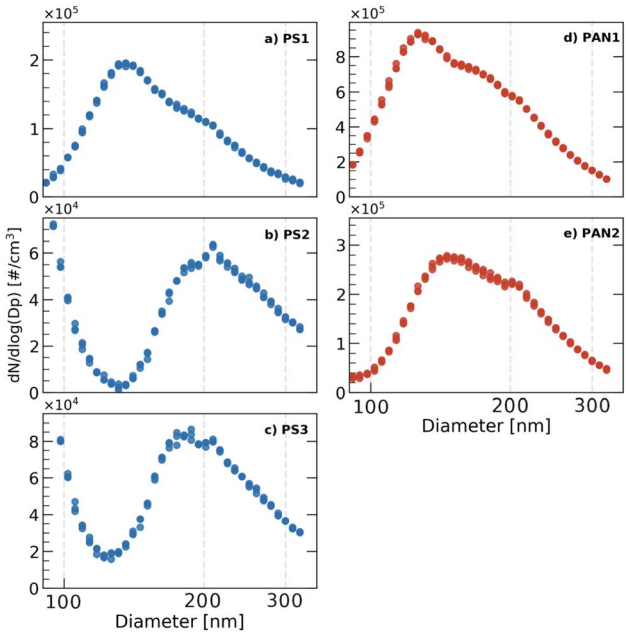

Fig. 2 Size distributions of PS (left, in blue) and PAN (right, in red) samples over the range 90–322 nm. Measurements were repeated 3 times. Vertical lines are placed to guide the eye and denote the 100, 200 and 300 nm diameters. Note different y-axis range on panels.

2.2.2 Horizontal ice nucleation chamber (HINC). In this study, we used HINC[73,74] to investigate the IN properties of model NPs. HINC is a continuous-flow diffusion chamber in which samples are exposed to varying RH and T conditions. The interior of the chamber is composed of copper walls lined with a sheet of glass-fiber filter paper (66217, Pall Corporation), which is wetted with deionized water prior to the experiments, and serves as a water vapour reservoir to maintain the desired RH. The copper chamber wall temperatures are controlled by two external recirculating ethanol chillers (ProLine RC890,

Lauda). Four thermocouples embedded in each wall with an uncertainty of ±0.1 K monitor the temperature. During the experiment, a thin ice layer forms at the inner surface of both wetted filter papers at subfreezing temperatures and remains at ice saturation condition ($RH_i = 100\%$). A temperature gradient is then established between the top and bottom walls ($T_{top} > T_{bottom}$). Due to the combination of the non-linear saturation vapour pressure as a function of temperature (Clausius–Clapeyron equation[75]) and the linear diffusion gradient between the plates, a region of supersaturation can be established at the centre of the chamber.[73] A laminar flow of nitrogen gas (F_{sheath}) is sustained inside the chamber and controlled by a mass flow controller (MFC, G-Series, MKS Instruments). The monodispersed sample flow F_{sample} containing the size-selected NP particles is injected in the centre, where the temperature remains constant such that F_{sample} is layered by F_{sheath} in the centreline. Before being injected into the chamber, the total number of particles up-stream of HINC was measured by a condensation particle counter (CPC, Model 3772, TSI Inc.) at a flow rate of 1 L min^{-1}. An optical particle counter (OPC, GT-526S, MetOne) placed downstream of the chamber detected the size-resolved concentrations of particles that exit the HINC. The size bins applied by the OPC were 0.3, 1, 3, 4, 5, and 6 μm and are used to distinguish water from ice for the experiments above 235 K. Below 235 K, only ice crystals are expected, therefore phase discrimination by size was not needed. Another MFC regulated the flow passing through the OPC (F_{OPC}, constant at 2.83 L min^{-1}). The aerosol-containing sample flow (F_A) drawn into HINC was set to approximately 0.22 L min^{-1} by adjusting F_{sheath} and keeping the OPC flow fixed. This results in preserving the ratio F_A to F_{sheath} at about 1 : 12 to maintain the laminarity and position of the sample flow.[74] The residence time τ of the aerosol flow in the chamber was approximately 11 seconds at the conditions listed above. The calibrated residence time was sufficient for the NPs to nucleate ice and grow to sizes detectable by the OPC, while minimizing losses due to gravitational settling.[74] Water droplet and ice crystal growth by diffusion of water vapor were calculated based on Rogers and Yau (1989),[76] assuming the entire residence time aerosol flow spent in HINC was used for diffusional growth. Experiments were conducted at temperatures between $T = 218$ and 243 K at 5 K intervals. To determine whether the HNT threshold influenced the ability of NPs to act as INPs, we also tested two temperatures above HNT (relevant for mixed-phase clouds).

In this study, ice crystal discrimination from inactivated aerosol particles and water droplets was based entirely on the optical diameter of the particles measured by the OPC downstream HINC. This was made possible because for the same temperature and saturation, the saturation vapor pressure of ice is lower than that of water,[66] and the growth of ice crystals is favored over water droplets. Homogeneous freezing experiments (see Appendix B) were conducted to compare the onset of freezing observed in HINC to theoretical values parameterized in the literature.[1] The tests were conducted with ammonium nitrate (AN, NH_4NO_3), a salt that possesses no heterogeneous IN abilities and is expected to freeze homogeneously. At $T \leq 235$ K, where water droplets freeze homogeneously, the OPC size bin with particle optical diameters >1 μm was chosen as the threshold to detect ice crystals from inactivated particles. 1 μm is above the size of the NPs entering HINC (200 nm) but at the same time small enough to detect ice crystals that nucleated along the chamber path. At warmer temperatures ($T > 235$ K), however, both supercooled water droplets and ice crystals can form. To avoid misclassification of water droplets as ice crystals, it was necessary to use a higher size threshold. At these temperatures, we used the 5 μm OPC channel instead. AN experiments at $T = 238$ and 243 K were used to identify the relative humidity at which the water droplets grow to sizes larger than 5 μm. This relative humidity is referred to as water droplet survival (WDS). Data points that fall above the WDS relative humidity are not considered to represent heterogeneous IN because water droplets and ice crystals can be co-detected by the OPC in this size channel (see Fig. 14). However, it is impossible to exclude that heterogeneous ice formation could occur simultaneously with or after droplet grows to sizes larger than 5 μm.

Previous laboratory validation experiments confirmed the accuracy of the thermodynamic conditions of temperature (T)[74] and relative humidity with respect to water (RH_w)[17] in HINC. Temperature uncertainties lie at T ±0.4 K while relative humidity uncertainties across the aerosol lamina is a function of T and RH_i at the center and the ratio F_A to F_{sheath} and are approximately RH_i ±3% (saturation ratio with respect to ice of ±0.03).[17,74]

2.2.3 Data analysis. During the IN experiments, frost can detach from the filter paper of the chamber walls, giving rise to additional particles falsely counted as nucleated ice crystals in the OPC channels. In order to correct for these false contributions, background measurements were made before and after each sampling period with a particle-free flow sampled by HINC for 5 minutes before and after each measurement at the target T and RH_i. A linear interpolation of the background counts was then subtracted from the data of all measured values (see Lacher *et al.*[74] for more details) to deduce the corrected ice counts.

The ratio of the ice crystal number to the total aerosol particle number was derived from the counts of the OPC and the CPC (eqn (1)), referred to as the aerosol particle activated fraction (AF).

$$AF = \frac{\#\text{ice crystals (OPC)}}{\#\text{total particles (CPC)}} \quad (1)$$

We used an AF value of 0.2% to represent the onset formation of ice, where the signal is sufficiently higher than the background noise (signal at low RH, where IN is absent, see the red horizontal dotted line in Fig. 11, Appendix A) and is corrected for noise.

2.3 Particle size distribution

The size distribution of the NPs was measured with the same differential mobility analyzer presented above with multiple charge correction applied. The DMA was operated with a sheath flow of 8 L min^{-1} and sample flow rate of 2.5 L min^{-1}, which

allows for testing the diameter range between 9 and 322 nm. The number of particles in each size bin was then counted by a CPC operated at a constant flow rate of 1 L min^{-1}. The particle size distributions are shown in Fig. 2. Since a mode of particles appeared at 200 nm for all samples, we size selected 200 nm mobility diameter particles for our ice nucleation experiments.

For our experiments, particles larger than 200 nm occurred exclusively on the down-slope of the particle size distribution or at the mode (only for PS2). This should reduce the number of doubly and triply charged particles sampled by HINC. We approximated the proportion of doubly and triply charged particles for our size selection conditions of $F_A = 2.5$ L min^{-1} and $F_{sheath} = 8$ L min^{-1} at 26.4% and 12.1% respectively.[77]

2.4 Surface characteristics

The surface morphology of the NPs was visualised using scanning electron microscopy (SEM, Zeiss Merlin). For each sample, a drop of concentrated solution (without any previous dilution or size selection) was placed onto a carbon sticker and dried in a clean environment overnight. Prior to the analysis, the sticker was coated with a 4 nm layer of Pd/Pt (Sputter Coater CCU-010, Safematic). SEM was employed at a low voltage of 2 to 5 kV to avoid damaging the sample, using secondary-electrons and in-lens detectors.

2.5 Water affinity (DVS)

Dynamic (water) vapor sorption (DVS, Model Advantage ET1, Surface Measurement Systems Ltd) is a gravimetric sorption technique that allows for the measurement of vapor absorption on a surface by varying the vapour concentration surrounding the sample. DVS measurements were performed on the NPs samples to analyze the surface characteristics (hydrophilicity) and porosity. Each DVS measurement was performed over 5 days at a constant temperature of 298.5 K, covering the range between 0 and 90% RH_w. First, the concentrated aqueous samples were dried by diffusion (*i.e.* evaporate water in the sample solution in a clean environment) to remove moisture and measure the mass of the dry samples. The dry samples were then exposed to a cycle of increasing (to measure water adsorption mass at RH_w 0–90%) and decreasing (to measure water desorption mass at RH_w 90–0%) water vapour pressures. The sample mass was probed at 10% RH_w steps after 360 minutes. Depending on the morphology of the particles (surface area and pore structure[78,79] and their chemical composition[80]), particles have different isotherm characteristics. The water uptake is expressed as the relative mass change difference between the (dry) sample mass at $RH_w = 0\%$ and the moist sample mass at the probed RH_w. The resulting water vapor sorption and desorption isotherms of the NPs are important parameters for determining the water affinity of the particles and the existence of porous structures where water can condense for PCF to occur. Additionally, the Gibbs free energy released during the DVS measurements also allow an estimation of the specific surface area of the NPs, which is expressed in $m^2\ g^{-1}$.

3 Results and discussion

3.1 Particle characterisation

3.1.1 Shape and surface morphology of model nanoplastics. SEM images were taken to depict the surface morphology and roughness of the NPs (Fig. 3). Overall, the particles deviate from a perfect spherical shape and exhibit varying degrees of surface irregularities across the samples. PS1 and PS2 demonstrate a consistent pattern of small, regularly-spaced protrusions. In contrast, PS3 display both deeper indentations and larger, irregularly-sized bumps ('raspberry morphology').[71] PAN1 possesses a relatively smooth and near-spherical geometry. While PAN2 maintains a comparable level of smoothness, the particles exhibit a more angular, less spherical profile.

3.1.2 Water uptake by model nanoplastics. The water vapour sorption isotherms of all NP samples observed from $0\% \leq RH_w \leq 90\%$ reveal the hydrophilicity of the particles (adsorption process, Fig. 4) and the surface roughness or porosity (desorption process, Fig. 5) if hysteresis is observed. The PAN NPs took up more water than PS NPs at lower-intermediate RH_w (0–60%, Fig. 4), which can be attributed to the polar nitrile functional groups the PAN surface but absent in PS. At $RH_w > 60\%$, PS2 and PS3 showed a steep increase with PS2 having a lower net uptake than PS3 at

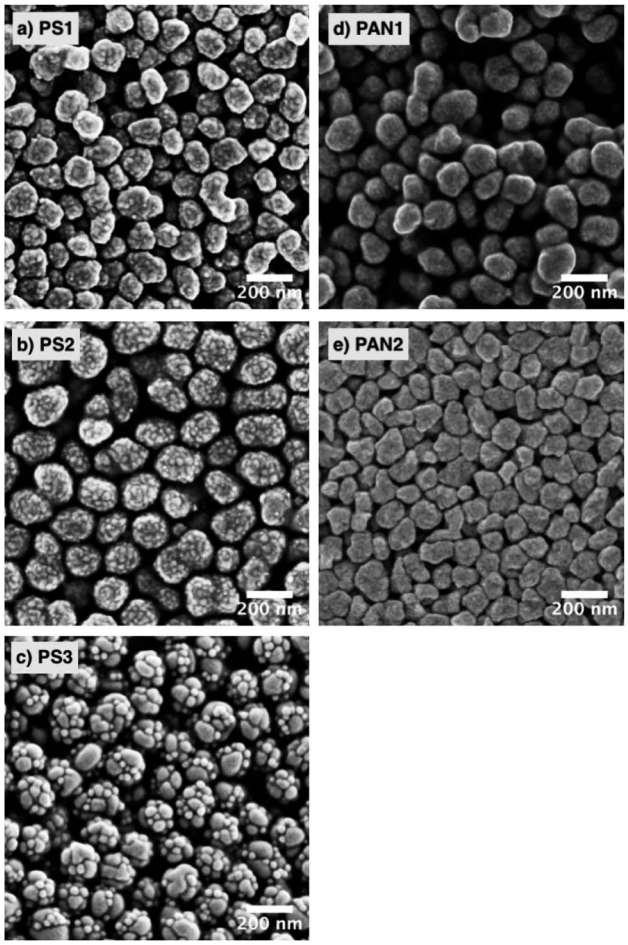

Fig. 3 SEM images of PS (a)–(c) and PAN (d) and (e).

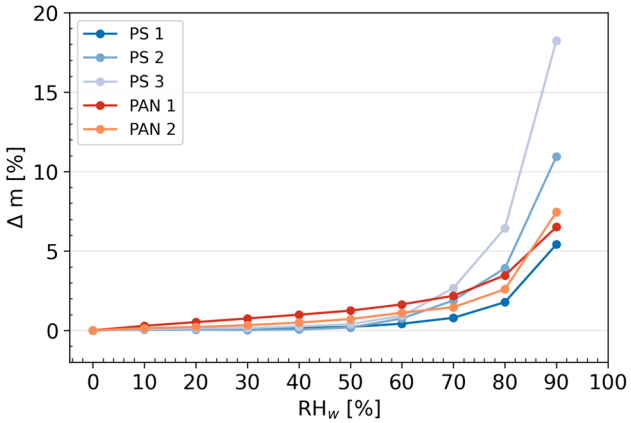

Fig. 4 Water vapour uptake isotherms shown as relative sample mass change as a function of RH_w measured by DVS at $T = 298.5$ K. Data points represent water uptake at quasi-equilibrated relative humidity conditions. The curves are linear interpolations between the points. Each curve represents once one adsorption and one desorption cycle taking a total of 5 days per sample.

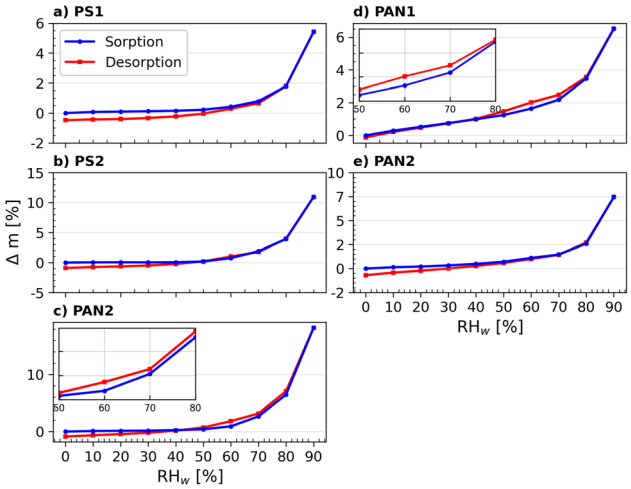

Fig. 5 Water vapor uptake and loss isotherms shown as relative sample mass change as a function of RH_w measured by DVS at $T = 298.5$ K. Data points represent water uptake at quasi-equilibrated relative humidity conditions. The curves are linear interpolations between the points. Note different y-axis range on panels.

$RH_w = 90\%$. PS1 showed the lowest water uptake of all samples at $RH_w = 90\%$.

Micropores (pores with diameter < 2 nm) can influence water uptake at $RH_w < 40\%$. The sorption isotherms suggest that the PAN NPs samples could have more surface micropores than PS, allowing more water to be adsorbed at low RH_w. Additionally, the polymer chains of PAN includes nitrile groups, which are polar and could favor interactions with water molecules. At higher RH_w, however, this water uptake mechanism is likely outcompeted by the larger surface area due by the presence of concave and convex surface structures of PS2 and PS3 (see Fig. 3). These features effectively translate into a larger surface area (see Table 1), allowing more water to be adsorbed, including multilayer water absorption. The PS samples did not have micropores, as indicated by the flat adsorption curves at $RH_w < 40\%$. In addition, PS1 lacked the large crevasses of PS2 and PS3, and as a result, it did not take up water as effectively as the other model NPs.

Table 1 Specific surface area in $m^2\ g^{-1}$ of the NP samples estimated from the release in Gibbs energy during the DVS measurements

NP sample	Specific surface area ($m^2\ g^{-1}$)
PS1	190.53
PS2	368.92
PS3	614.98
PAN1	33.06
PAN2	262.17

The desorption isotherms for each individual sample are shown together with the adsorption experiments in Fig. 5 to determine the presence of a hysteresis (*i.e.*, when the absorption and desorption curves do not coincide). Hysteresis is observed in the region ≥40% for the samples PS3 and PAN1. Hysteresis between RH_w values of 60% and 90% indicate the presence of mesopores (pores with diameters between 2 and 50 nm) in the sample,[81] where the water uptake mechanism is capillary pore condensation. The water condensed in the pores experiences higher saturation than the surrounding air and does not evaporate immediately as RH_w decreases during the measurements, leading to hysteresis. All other NP samples (PS1, PS2 and PAN2) did not show hysteresis, suggesting that mesopores are either negligible or absent on the particle surface. Following the classification recommendations according to IUPAC,[81] it is possible to classify the shape of the uptake curves for PS3 and PAN1 as type-IV(a) isotherms. Although the increase in mass at low RH_w (≤20%) is not pronounced, there is a slow rise at intermediate RH_w (20–80%) followed by a sharp increase at high RH_w (≥80%). Additionally, the desorption curve presents a hysteresis typical to this type of isotherm. PS1, PS2 and PAN2 have similar adsorption curves, but they do not present hysteresis in the desorption curve and can therefore be classified as type-III isotherms.

We note an artifact present in the probed mass at $RH_w = 0\%$, where the dry sample mass of the desorption isotherm is lower than the sorption isotherm. While this artifact should not prevent us from concluding the presence of hysteresis, some exploration as to why this occurred is warranted. Most likely, the bulk characteristics of the dried NPs changed after a full cycle of sorption and desorption (see Appendix C). When a drop of aqueous buffer solution evaporates, the NPs form a homogeneous film-like structure (Fig. 15) and only small cracks are visible. However, after exposure to the DVS measurement cycle, new cracks formed on the bulk surface (Fig. 16), exposing new surfaces to the controlled air inside the DVS and could evaporate previously trapped water that was not evaporated in the drying phase from the previous cycle(s). While the mass of dry NPs (~1 mg) was sufficient for DVS experiments, it was too small to quantify the surface area of the NPs by using other techniques, such as N_2-BET, which requires approximately 1 g of material.

3.2 Ice nucleation activity of model polystyrene nanoplastics

An overview of the saturation ratio with respect to ice (S_i) at the onset of ice nucleation given at AF 0.2% (Fig. 10–12) for the PS

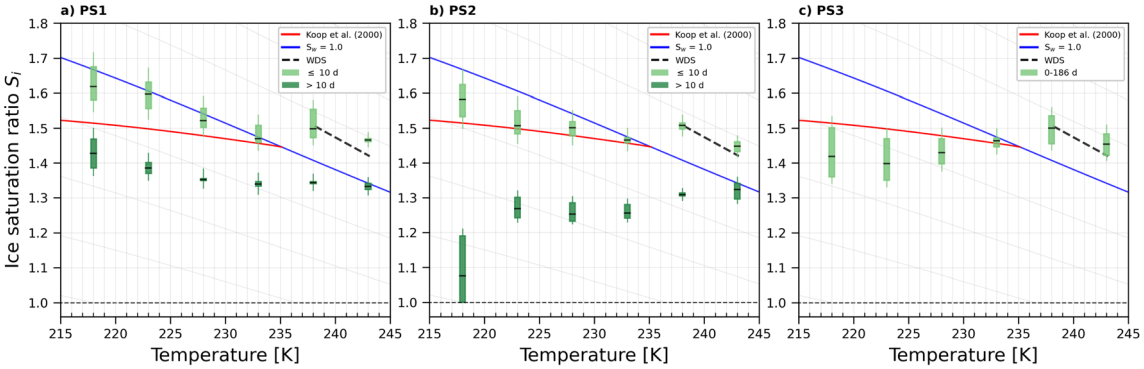

Fig. 6 Onset S_i (0.2% AF) for ice formation for 200 nm PS1 (a), PS2 (b) and PS3 (c) NPs. Each range encloses all experiment results (2–7 repetitions per NPs type at the specified temperature). For PS1 and PS2, light green boxes represent fresh NPs (<10 days old), while dark green box presents NPs suspended in water >10 days (up to 80 and 36 days for PS1 and PS2 respectively). PS3 was tested in the range 0–186 days. Black horizontal lines indicate mean value of each range. The blue line denotes water saturation ($S_w = 1.0$) and the parallel grey lines water saturation ratio in decrements of 0.1,[82] the red line is the parameterisation for homogeneous freezing of solution droplets at a nucleation rate coefficient of 10^{10} cm^{-3} s^{-1}.[1] The black dashed line represents water drop survival (WDS) conditions above which we cannot confidently distinguish between an ice crystal and water droplet (upper detection limit of instrument). Vertical error bars represent calculated variations in the saturation across the aerosol layer thickness in HINC.[17] Temperature uncertainty is ±0.4 K.[74]

samples (d_{el} = 200 nm) is shown in Fig. 6. Generally, PS1 (Fig. 6a) and PS2 (Fig. 6b) had similar IN activities for samples that were <10 days old in diluted aqueous suspensions (referred to as young). Heterogeneous ice nucleation was not observed for young PS1 and PS2 samples as shown by the ice nucleation onset being above the WDS line where ice crystals cannot be distinguished from water droplets (black dashed line in Fig. 6) or at/above the homogeneous freezing threshold for solution droplets (red line in Fig. 6). PS3 samples showed some heterogeneous ice nucleation ability at T < 233 K, but the ice onsets observed were close to that required for homogeneous freezing, as such do not promote ice formation and are poor INPs for all temperatures tested here. For samples >10 days in the dilute suspensions (referred to as old), the IN activity was significantly improved (lower onset S_i) for PS1 (0–80 days) and PS2 (0–36 days), but remained within the same range as the young samples for PS3. For this reason, the data presented in Fig. 6c represent NPs at both ages (0–186 days).

3.3 Ice nucleation activity of model polyacrylonitrile nanoplastics

The onset S_i for ice nucleation of the d_{el} = 200 nm PAN samples were quite variable at a given temperature as shown in Fig. 7. PAN1 could nucleate ice heterogeneously only at $T \leq 228$ K. At $T = 233$ K the PAN1 froze at S_i required for homogeneous ice nucleation. At T = 238 K, PAN1 NPs could have nucleated ice by immersion freezing, as the observations border the upper detection limit of the WDS and have reduced confidence. At $T = 243$ K, the ice onset lies at/above WDS conditions. Overall PAN1 samples were ice active only in the cirrus temperature regime at $T \leq 228$ K and PAN2 could nucleate ice heterogeneously at all tested temperatures. In contrast to the PS, there was no distinction in ice nucleation observed based on age of the dilute suspensions for both the PAN samples. Therefore the data for young and old samples are given by the range plotted in Fig. 7. PAN1 was tested in the range 0–79 days and PAN2 between 0 and 99 days.

3.4 Discussion

All three of the young PS NP samples displayed poor to no ice nucleation ability. The PAN samples, by contrast showed significantly better IN exhibiting lower onset S_i. This can be attributed to the difference in chemical composition of the two NP samples, with the PAN having a polar nitrile group which would stabilise the formation of an ice germ at these nitrile sites, thus promoting ice nucleation. The higher hydrophilicity of the PAN samples is further supported by their increased water uptake in the range RH_w 0–60%, compared to the PS samples in the same range (Fig. 4). The PAN2 sample showed a slightly higher IN ability than PAN1. For similarly composed particles, the surface morphology plays a role in promoting ice nucleation by providing an active site to stabilise ice germ formation. In fact, with black carbon particles, it has been shown that surface morphology is the more important predictor for ice nucleation compared to the surface chemistry of the particles.[83] The water uptake onto particles at high RH_w is typically due to the surface morphology and total surface area of particles (see 3.1.2), rather than indications of water vapour interactions with the molecular composition of the sample. The PAN2 sample takes up more water at RH_w 90%, supporting more complex surface morphology (less spherical, more angular) compared to PAN1, and the better ice nucleation ability of PAN2.

All five samples had morphological features (*i.e.*, they were not purely smooth and spherical) (see 3.1.1), which can ultimately define their IN activity.[84] For instance, the PS3 and PAN1 samples showed overlapping ice onset S_i ranges, where ice nucleation only occurred at temperatures below the HNT. The sorption and desorption curves obtained from the DVS measurements confirmed the similarities in water uptake between these two samples. Although PS3 NPs had a higher total water uptake (likely due to the larger total surface area), both PS3 and PAN1 NPs presented hysteresis in their respective desorption curves, which is an important factor indicative of the porosity of the samples. In previous ice nucleation studies,[70,84,85] the presence of mesopores was deemed as a key element for ice nucleation to occur *via* the

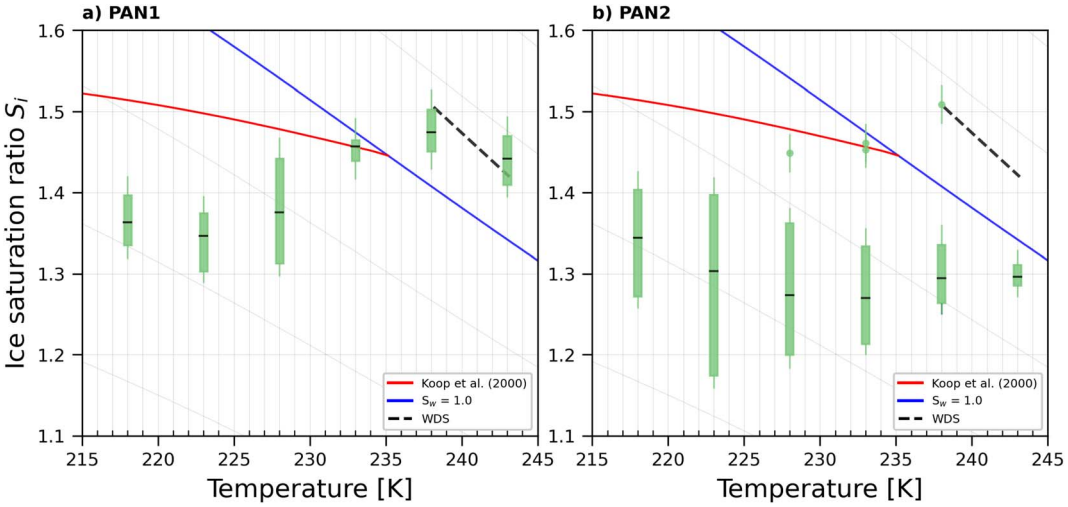

Fig. 7 Onset S_i (0.2% AF) for ice formation for 200 nm PAN1 (a) and PAN2 (b) aerosol particles. Each range encloses all experiment results (4–8 repetitions) that were obtained with each sample at the specific temperature. PAN1 and PAN2 were tested in the time range 0–79 and 0–99 days respectively. Outliers, represented by single data points, are present in PAN2 at $T = 228$, 233, and 238 K. The black horizontal lines are the mean value of each range. The blue line denotes water saturation ($S_w = 1.0$) and the parallel grey lines water saturation ratio in decrements of 0.1,[82] the red line is the parameterisation for homogeneous freezing of solution droplets at a nucleation rate coefficient of 10^{10} cm^{-3} s^{-1}.[1] The black dashed line represents water drop survival (WDS) conditions above which we cannot confidently distinguish between an ice crystal and water droplet (upper detection limit of instrument). Vertical error bars represent calculated variations in the saturation across the aerosol layer thickness in HINC.[17] Temperature uncertainty is ±0.4 K.[74]

PCF mechanism, as they favour water condensation at lower saturation due to the inverse Kelvin effect.[70] The condensed water within the pores can freeze homogeneously if the temperature is below HNT and the pore diameter is large enough to accommodate the ice germ.[84] Above HNT, the pore water can freeze heterogeneously if there is the presence of an active site (such as a polar functional group) stabilizing the ice germ.[70] Freezing of water in the pores can subsequently trigger macroscopic ice growth, resulting in ice crystal formation. Further indication that PCF is occurring in PAN1 and PS3 is supported by the shape of the AF curves shown in Fig. 9 and 10 in the Appendix A. At $T <$ HNT, the AF steeply increases when the critical S_i is reached, which is consistent with the PCF mechanism that requires pores to be filled first at subsaturated conditions with subsequent freezing only after pore filling.[70] We attribute the freezing mechanism of PS1, PS2, and PAN2 NPs to deposition nucleation type mechanisms, supported by the DVS measurements which showed no hysteresis in the desorption isotherms, meaning that the pores could be too few or too shallow or large to experience the inverse kelvin effect and retain water efficiently. The AF curves of PS1, PS2, and PAN2 are shown in Fig. 11–13 respectively, where the AF increases below water saturation for all tested temperatures, supporting deposition mode ice nucleation. However, we can not exclude that an undetectable amount of hysteresis is present and a combination of adsorption freezing[86] and deposition nucleation could be occurring.

Another finding is that PS1 and PS2 NPs showed heterogeneous IN activities exhibited by the significantly lower onset S_i when the samples were old (remained in suspension for longer than 10 days). NPs stored in the stock buffered solution are stable and should not undergo morphological or chemical changes.[71] In the diluted suspension the buffer concentration should be negligible (dilution factor 1000), and if storing under these conditions induce any changes to the particle is not known. Given that these particles were stored in water, in conditions exposed to room light and indirect sunlight for weeks, without being in an inert atmosphere, one cannot exclude multiple possibilities of processes that could have occurred in these suspensions. These include ageing mechanisms such as chemical oxidation through weak hydrolysis, light irradiation, and biodegradation of the water.[87] It has been shown when a water–air interface is present even in dark conditions, OH radicals form in the bulk solution over several weeks of storage.[88] These OH radicals could then oxidise the plastic particles making them more hydrophilic and ice nucleation active as in the case of our PS1 and PS2 samples that were initially not ice nucleation active. This effect could be muted for the PS3 samples as these young samples were already as active as the old PS1/PS2 samples. Storage for weeks in a still water suspension could also result in leaching of any additives. For instance our NP samples have palladium cores embedded in them for the synthesis procedure, and over weeks of storage in water suspensions, even though not expected,[71] we cannot fully exclude some palladium albeit small percentages leaching out. If this occurs even in a small fraction of the particles, water molecules could exchange with the palladium and make the particles IN active upon exposure to supercooled temperatures. Biodegradation of the water could occur if the warm room temperature and still water conditions promote bacterial growth resulting in adsorption of organics to the plastic particle surface (ecocorona formation).[69,89] A source of NP particles in drinking water has been attributed to storage in plastic bottles[90] where it was suggested that NPs leach out of the packaging in contact with the water resulting in concentrations of up to 240 000 particles per L of water.[90] This demonstrates that plastic may not be as stable water. All the above potentially result in changing ice

nucleation activity.[18] Changes to the surface of the particle could lead to increased hygroscopicity or new surface impurities such as cracks and/or pores, both of which would result in ability to nucleate ice heterogeneously at lower S_i. The enhanced IN ability of the old PS1 and PS2 NPs is also supported by the shape of the AF curves visible in Fig. 11 (a, PS1) and 12 (b, PS2). The aged samples (red mean) clearly shows ice formation beginning at much lower S_i than young samples. Further characterisation of the aged samples for changes in morphology *via* SEM or DVS was not possible from the diluted suspensions because enough material could not be recovered, and the change in IN ability reported here of the aged samples was happenstance observation. More detailed experiments in the future will focus on understanding this phenomenon (*e.g.*, including water bodies found in different aquatic environments such as lakes or oceans) by producing large sample sizes of synthetic NPs, but are beyond the scope of the current work. Here we emphasize that with respect to IN activity, the NP samples become modified after being stored in water suspensions, suggesting that water should not be treated as a chemically inert substance for aerosolization, a fact which has also been observed for mineral dust particles.[91,92] For feldspar dust particles, leaching of minerals from the particles being replaced with protons from water can result in enhanced IN activity.[91]

The results from this work cannot be directly compared to two existing ice nucleation studies of MnP are already published.[19,21] First because different particle types (compositions) and temperature ranges have been studied. Second, because the total surface area of the particles in the their cloud droplet or ice crystal are different from ours. Since Ganguly and Ariya[19] and Seifried *et al.*[21] used droplet freezing methods, these typically have much more than the equivalent surface area of one aerosol particle, yielding warmer freezing temperatures. Nonetheless, their conclusions that plastic particles can indeed nucleate ice heterogeneously in their investigated temperature regime (265–243 K) is in agreement with our results that NP also nucleate ice between 243 and 218 K. In cloud water samples and in the environment, MnPs not only have different compositions, but also morphologies[22] that include sharp edges (fibers) and potentially cracks and crevices due to weathering in the environment. These morphological features may be relevant for ice nucleation by deposition or PCF explored in this work. Such features are thought to create additional active sites for ice to form thus enhancing particle ice nucleation activity. These active sites can be pores of different shapes and sizes where water can condense under the capillary effect. However, the mixing state of the particles is important to determine if these features can enhance ice nucleation. For example, it has been shown for deposition mode active dust[93,94] and soot particles[95,96] that if they contain small amounts of coating from nitrates or sulfates their ice nucleation activity can be suppressed.

3.5 Atmospheric implications

The higher IN activity of the PAN and aged PS samples imply that they could initiate ice cloud formation at conditions similar to a variety of dust particles,[97] for example illite, the most abundant component of airborne dust[8,97] nucleates ice between S_i 1.1–1.4

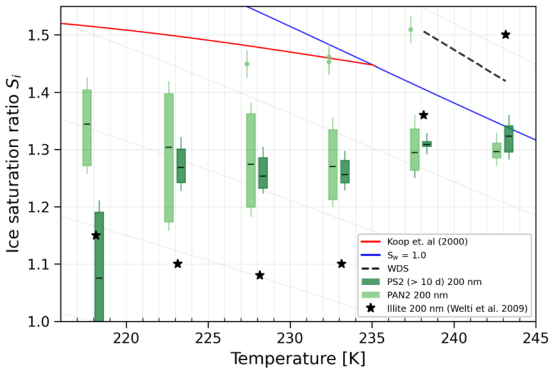

Fig. 8 Mean onset S_i (0.2% AF) for ice formation for 200 nm PAN2, PS2 (>10 days), and illite (from Welti *et al.*[97]) particles. The blue line denotes water saturation ($S_w = 1.0$) and the parallel grey lines water saturation ratio in decrements of 0.1.[82] The red line is the parameterisation for homogeneous freezing of solution droplets at a nucleation rate coefficient of 10^{10} cm^{-3} s^{-1}.[1] The black dashed line represents water drop survival (WDS) conditions above which we cannot confidently distinguish between an ice crystal and water droplet (upper detection limit of instrument). Vertical error bars represent calculated variations in the saturation across the aerosol layer thickness in HINC.[17] Temperature uncertainty is ±0.4 K.[74]

(Fig. 8). The onset S_i for aged PS1 (Fig. 6a) ranges from 1.30 ($T = 233$ K) to 1.47 ($T = 218$ K). Aged PS2 (Fig. 6b) showed even lower onset S_i than PS1 as T decreases to 223 K. In particular, at $T = 218$ K, PS2 NPs showed a much lower S_i, with ice production starting at ice saturation (at $S_i = 1.0$). In Fig. 8 we show that illite samples from Welti *et al.*[97] are overall the most active INP at $T \leq 233$ K, as it can nucleate ice at the lowest S_i. At higher temperatures, PAN2 appears to be more IN active than illite. These results suggest that both young and old (aged) plastic particles may at certain temperatures compete with mineral dust particles for ice nucleation in the atmosphere. However, only comparing the onset S_i does not render NPs relevant for ice cloud formation in the troposphere. NPs could potentially be atmospherically relevant if their abundance is comparable to that of other known active INPs or if they are found in regions where other more abundant INPs are depleted (such as the Arctic or Southern Ocean where background naturally occurring INP concentrations are low).[18,59] Currently, NP concentrations in the atmosphere are uncertain, but newer studies quantifying airborne NPs are emerging.[64] Niu *et al.*[64] detected 30 ng m^{-3} of airborne PS particles in College Station, TX, USA. Using a density of 1.07 g cm^{-3} for PS, we estimate that at 233 K if 0.2% of the PS2 samples with a diameter of 200 nm are ice active at $S_i = 1.25$ (see Fig. 8), this results in an INP concentration of 1.7 L^{-1}. This is only a factor of 4 lower than the INP concentration measured at the same conditions in Storm Peak (7 L^{-1}) where mineral dust was thought to be the dominant INP.[98] In the future NP emissions are expected to increase and current estimates are already thought to be significantly underestimated.[35,99,100]

4 Conclusions

We investigated ice nucleation abilities of model NPs of two different polymers, polystyrene and polyacrylonitrile, with various surface morphologies as a function of temperature and

relative humidity. The ice nucleation ability of model PS1 and PS2 samples, was strongly related to the particle age in water before ice nucleation. Fresh samples (<10 days old) were not able to nucleate ice below homogeneous freezing conditions or above 233 K, while aged particles (>10 days old) were able to enhance the ice nucleation ability (*i.e.*, reduce the required onset S_i).

Model PS3 and PAN1 particles showed similar ice nucleation ability and a dependence on the HNT. We attribute this freezing mechanism to PCF as supported by the water adsorption/desorption measurements showing a hysteresis. PAN2 was able to nucleate ice at all investigated temperatures and did not show a hysteresis in the water adsorption/desorption properties, suggesting the absence of detectable porous features supporting classical deposition ice nucleation and not PCF as the mechanism of ice formation.

The ice nucleation experiments conducted here only present data on a limited number of NP variants. In the environment NPs will have a far greater variety of chemical compositions (such as polyethylene, polypropylene, and polyethylene terephthalate), sizes, morphologies and states of weathering. The results of this work serve to indicate that this emerging contaminant is complex with respect to its physicochemical properties and that future ice nucleation studies should focus on testing NPs with particles of different compositions and sizes. Additional experiments could also focus on the possible effects on ice nucleation of atmospheric weathering,[21] organic matter adsorption, and other chemical components found in the atmosphere that have the potential to change the surface characteristics and consequently ice nucleation activity of the NP particles.

Data availability

All the data supporting this article are available at: **https://doi.org/10.3929/ethz-b-000721162**.

Author contributions

ZAK and GL designed the experiment. DMM provided the NP samples. OG conducted the experiments and data analysis. OG, ZAK, and GL interpreted the data. CHD performed the DVS experiments and provided interpretation together with ZAK. OG and ZAK wrote the manuscript with contributions from GL. All authors contributed to reviewing and editing the article. ZAK supervised OG and GL.

Conflicts of interest

There are no conflicts to declare.

Appendix A: activated fractions

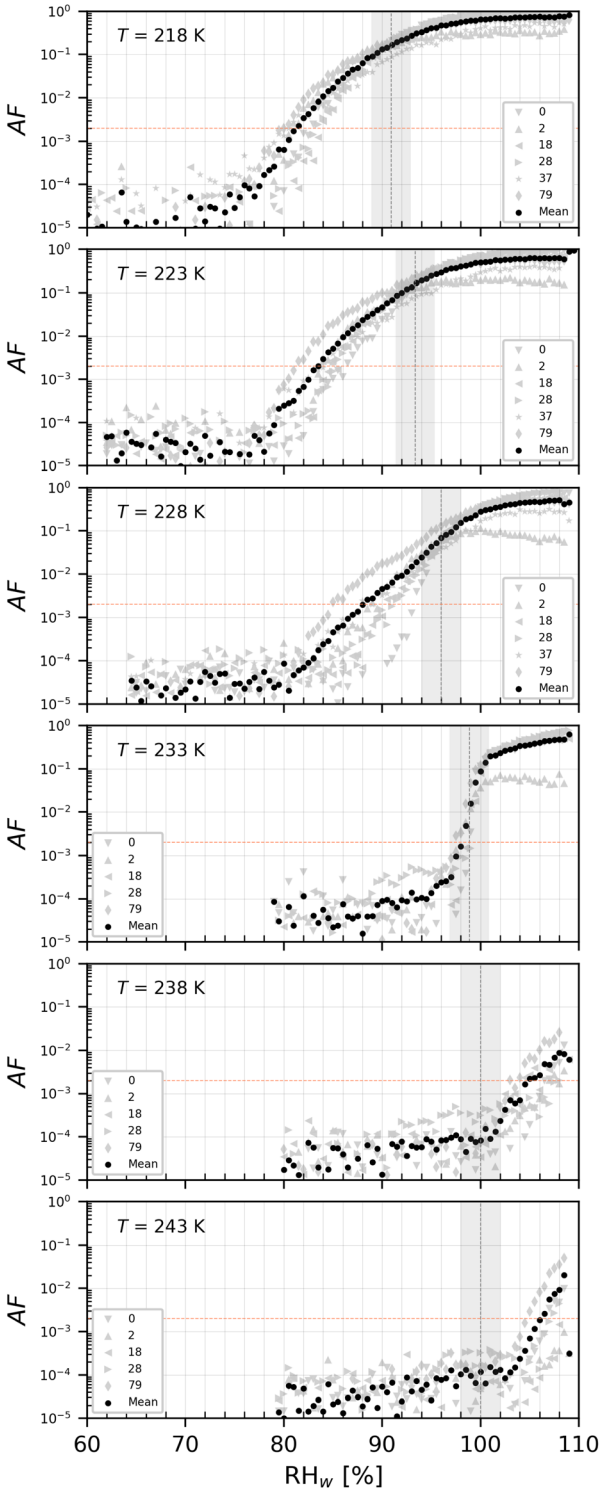

Fig. 9 AF as a function of RH_w at the given T for PAN1 with d_{el} = 200 nm. The numbers represent the age in days of the diluted suspension used to aerosolize the NPs. The black markers are the mean of all experiments. The vertical dotted line is the parameterisation for homogeneous freezing of solution droplets at a nucleation rate coefficient of 10^{10} cm^{-3} s^{-1} (at T < HNT) according to Koop *et al.*[1] and water saturation for T = 238 and 243 K.

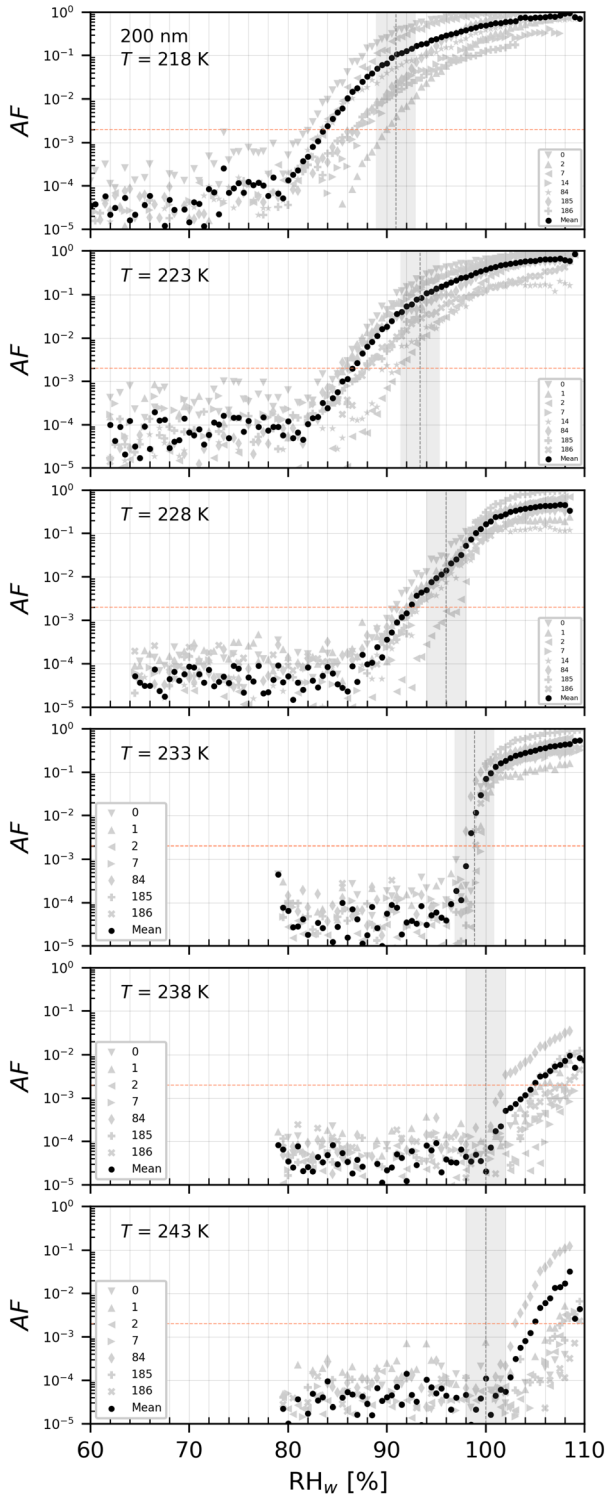

Fig. 10 AF as a function of RH_w at the given T for PS3 with d_{el} = 200 nm. The numbers represent the age in days of the diluted suspension used to aerosolize the NPs. The black markers are the mean of all experiments. The vertical dotted line is the parameterisation for homogeneous freezing of solution droplets at a nucleation rate coefficient of 10^{10} cm^{-3} s^{-1} (at T < HNT) according to Koop *et al.*[1] and water saturation for T = 238 and 243 K.

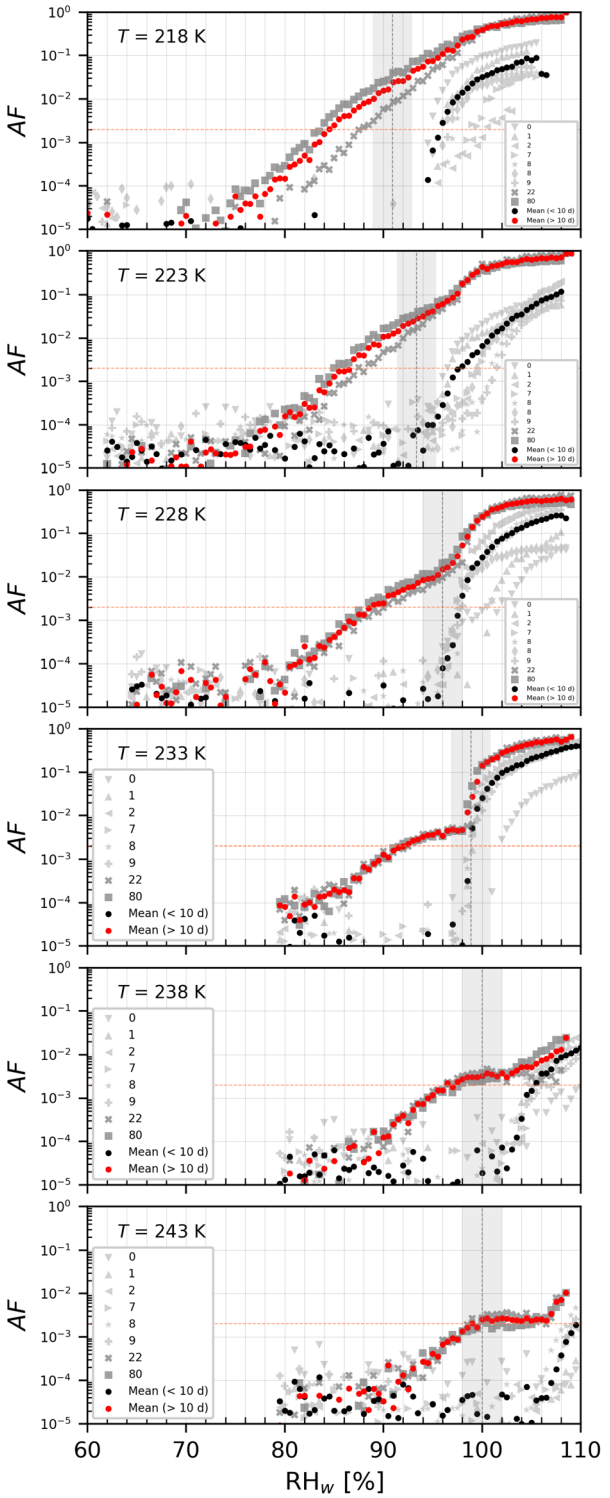

Fig. 11 AF as a function of RH_w at the given T for PS1 with d_{el} = 200 nm. The numbers represent the age in days of the diluted suspension used to aerosolize the NPs. The black and red markers are the mean of all experiments. The vertical dotted line is the parameterisation for homogeneous freezing of solution droplets at a nucleation rate coefficient of 10^{10} cm^{-3} s^{-1} (at T < HNT) according to Koop *et al.*[1] and water saturation for T = 238 and 243 K.

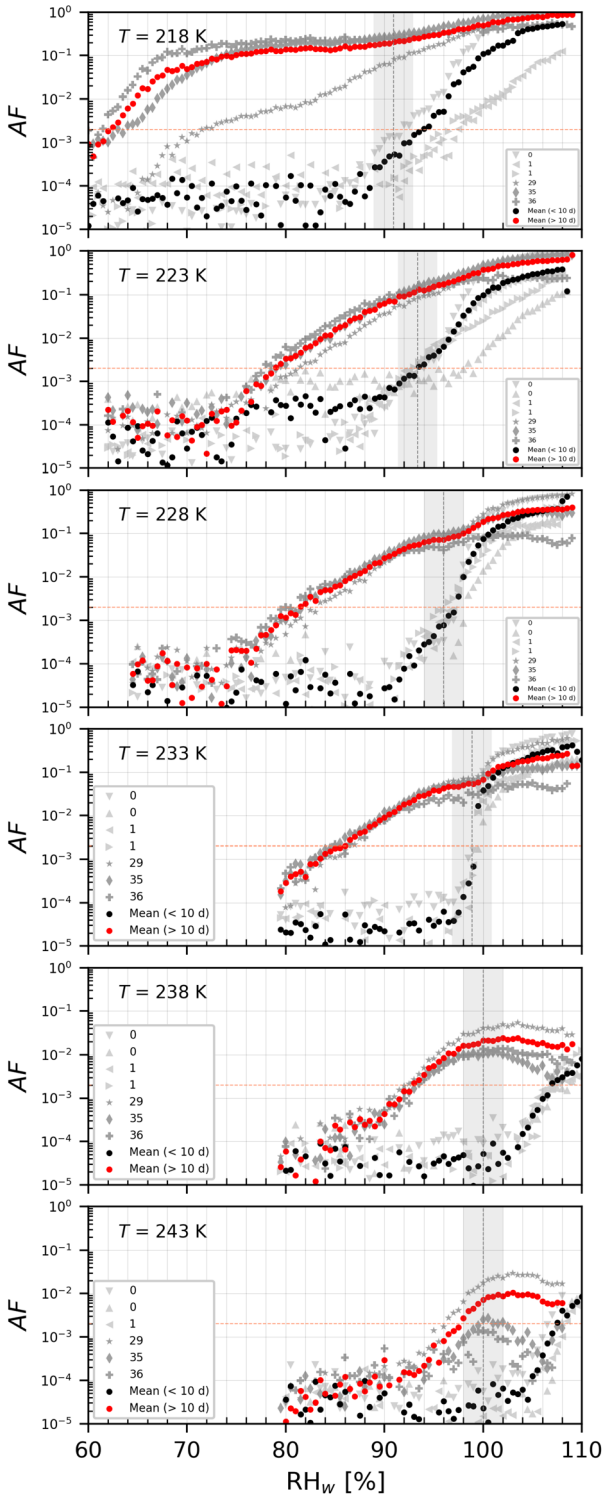

Fig. 12 AF as a function of RH_w at the given T for PS2 with d_{el} = 200 nm. The numbers represent the age in days of the diluted suspension used to aerosolize the NPs. The black and red markers are the mean of all experiments. The vertical dotted line is the parameterisation for homogeneous freezing of solution droplets at a nucleation rate coefficient of 10^{10} cm^{-3} s^{-1} (at T < HNT) according to Koop *et al.*[1] and water saturation for T = 238 and 243 K.

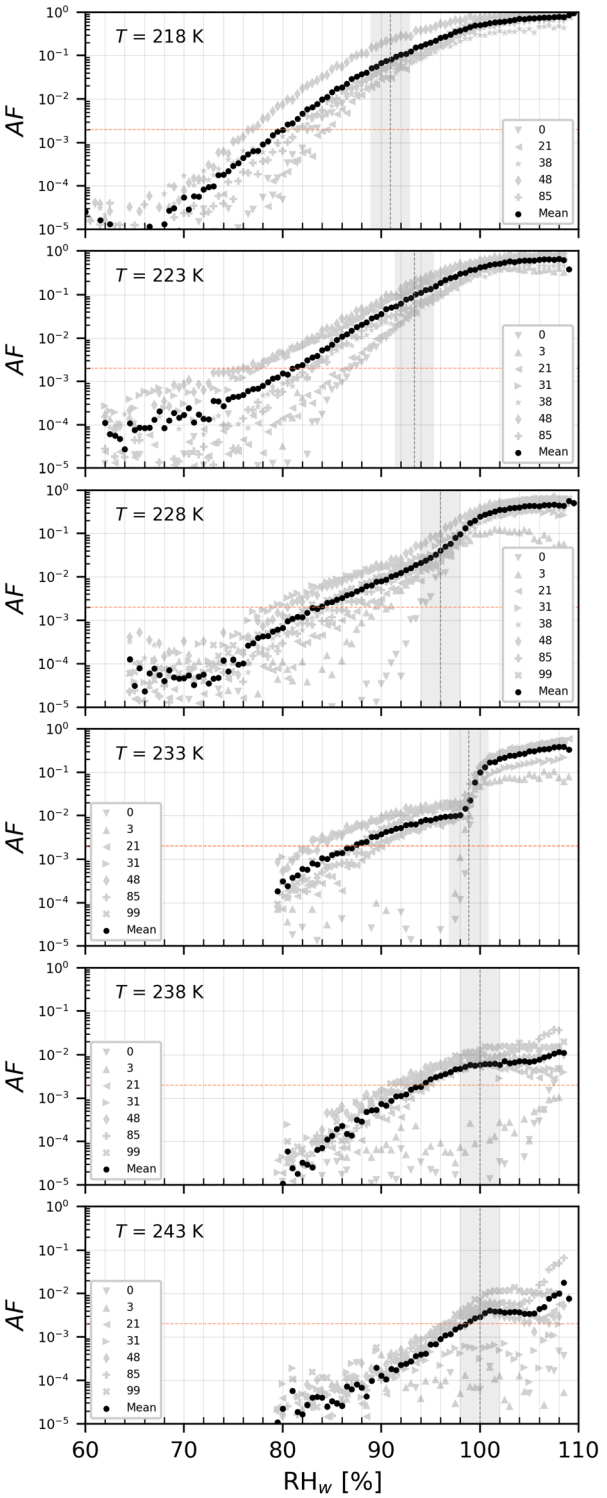

Fig. 13 AF as a function of RH_w at the given T for PAN2 with d_{el} = 200 nm. The numbers represent the age in days of the diluted suspension used to aerosolize the NPs. The black markers are the mean of all experiments. The vertical dotted line is the parameterisation for homogeneous freezing of solution droplets at a nucleation rate coefficient of 10^{10} cm^{-3} s^{-1} (at T < HNT) according to Koop *et al.*[1] and water saturation for T = 238 and 243 K.

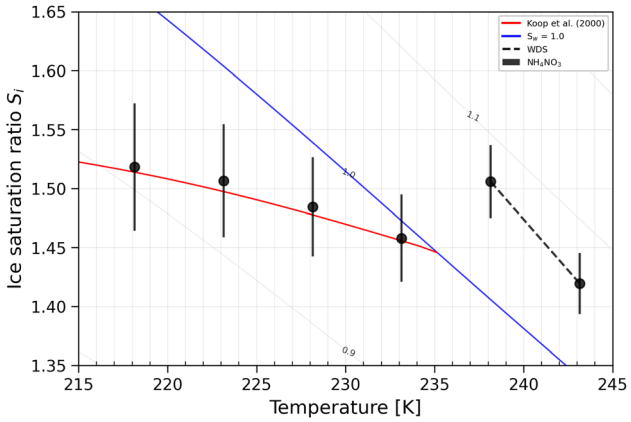

Fig. 14 Ice onset S_i ranges (0.2% AF) for 200 nm AN particles. The blue line denotes water saturation ($S_w = 1.0$),[82] the red line is the parametrization for homogeneous freezing of solution droplets at a nucleation rate coefficient of 10^{10} cm^{-3} s^{-1}.[1] The black dashed line represents WDS conditions. Vertical error bars represent calculated variations in the saturation across the aerosol layer thickness in HINC.[17] Temperature uncertainty is ±0.4 K.[74]

Appendix B: ammonium nitrate experiments

Ammonium nitrate (AN) solutions were used to conduct cloud droplet activation experiments and homogeneous freezing experiments. Cloud droplet activation is conducted to validate the accuracy of the water saturation reached inside HINC. AN was used because it is not expected to freeze at $T > 235$ K, therefore only forming liquid cloud droplets. At $T > 235$ K, AN experiments are also used to determine water droplet survival (WDS) in HINC, namely the RH_w conditions at which water droplets are detected by the 5 μm OPC channel. The WDS line (formed by the linear interpolation between the two points at $T = 238$, 243 K – the black, dashed line in Fig. 14) is considered as the maximum RH_w at which ice can be detected in our experiments. At $T < 235$ K, AN experiments are used to validate homogeneous freezing conditions. Ice formation should appear only at or above the curve that parameterise the homogeneous freezing of solution droplets.[1]

Appendix C: DVS artefacts

Fig. 15 illustrates the film-like structure of the compact NP after the water in the bulk solution is let dry. Fig. 16 illustrates the same film-like structure that is rearranged after it went through a complete cycle in the DVS.

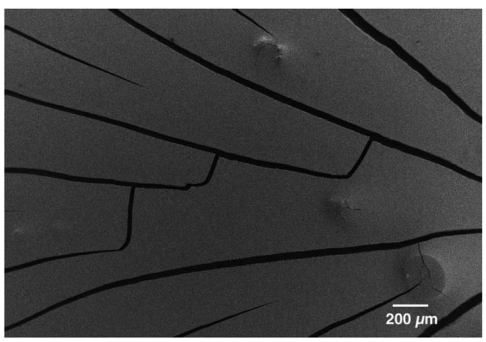

Fig. 15 SEM image of the compact NP after the solution was let dry.

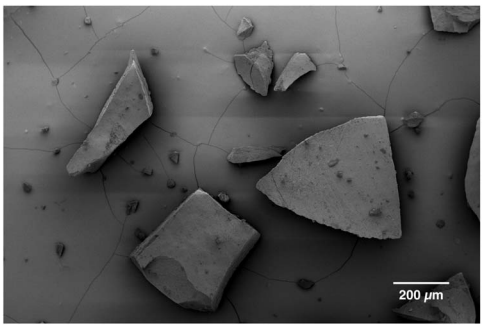

Fig. 16 SEM image of the compact NP after the DVS cycle.

Acknowledgements

We are grateful to the experimental atmospheric physics group at ETH Zurich for providing technical competence and help with instrument trouble shooting. We thank the Scientific Center for Optical and Electron Microscopy of ETH Zurich for providing direct access to the electron microscopy equipment. This work was supported by the Experimental Atmospheric Physics Professorship at ETH Zurich. D. M. M. was funded by the Swiss National Science Foundation, project number PCEFP2_186856.

Notes and references

1 T. Koop, B. Luo, A. Tsias and T. Peter, *Nature*, 2000, **406**, 611–614.
2 A. V. Matus and T. S. L'Ecuyer, *J. Geophys. Res.: Atmos.*, 2017, **122**, 2559–2578.
3 J. Mülmenstädt, O. Sourdeval, J. Delanoë and J. Quaas, *Geophys. Res. Lett.*, 2015, **42**, 6502–6509.
4 P. J. DeMott, A. J. Prenni, X. Liu, S. M. Kreidenweis, M. D. Petters, C. H. Twohy, M. S. Richardson, T. Eidhammer and D. C. Rogers, *Proc. Natl. Acad. Sci. U. S. A.*, 2010, **107**, 11217–11222.
5 U. Lohmann and J. Feichter, *Atmos. Chem. Phys.*, 2005, **5**, 715–737.
6 C. Hoose and O. Möhler, *Atmos. Chem. Phys.*, 2012, **12**, 9817–9854.
7 L. A. Ladino Moreno, O. Stetzer and U. Lohmann, *Atmos. Chem. Phys.*, 2013, **13**, 9745–9769.
8 B. J. Murray, D. O'Sullivan, J. D. Atkinson and M. E. Webb, *Chem. Soc. Rev.*, 2012, **41**, 6519.
9 A. Welti, Z. A. Kanji, F. Lüönd, O. Stetzer and U. Lohmann, *J. Atmos. Sci.*, 2014, **71**, 16–36.
10 A. Welti, U. Lohmann and Z. A. Kanji, *Atmos. Chem. Phys.*, 2019, **19**, 10901–10918.
11 E. C. Maters, D. B. Dingwell, C. Cimarelli, D. Müller, T. F. Whale and B. J. Murray, *Atmos. Chem. Phys.*, 2019, **19**, 5451–5465.

12 E. Gute, R. O. David, Z. A. Kanji and J. P. D. Abbatt, *ACS Earth Space Chem.*, 2020, **4**, 2312–2319.
13 B. G. Pummer, H. Bauer, J. Bernardi, S. Bleicher and H. Grothe, *Atmos. Chem. Phys.*, 2012, **12**, 2541–2550.
14 T. W. Wilson, L. A. Ladino, P. A. Alpert, M. N. Breckels, I. M. Brooks, J. Browse, S. M. Burrows, K. S. Carslaw, J. A. Huffman, C. Judd, W. P. Kilthau, R. H. Mason, G. McFiggans, L. A. Miller, J. J. Nájera, E. Polishchuk, S. Rae, C. Schiller, M. Si, J. V. Temprado, T. Whale, J. Wong, O. Wurl, J. Yakobi-Hancock, J. P. D. Abbatt, J. Y. Aller, A. K. Bertram, D. A. Knopf and B. J. Murray, *Nature*, 2015, **525**, 234–238.
15 V. R. Després, J. A. Huffman, S. M. Burrows, C. Hoose, A. S. Safatov, G. Buryak, J. Fröhlich-Nowoisky, W. Elbert, M. O. Andreae, U. Pöschl and R. Jaenicke, *Tellus B*, 2012, **64**, 15598.
16 D. A. Knopf, P. A. Alpert and B. Wang, *ACS Earth Space Chem.*, 2018, **2**, 168–202.
17 F. Mahrt, C. Marcolli, R. O. David, P. Grönquist, E. J. Barthazy Meier, U. Lohmann and Z. A. Kanji, *Atmos. Chem. Phys.*, 2018, **18**, 13363–13392.
18 M. Aeschlimann, G. Li, Z. A. Kanji and D. M. Mitrano, *Nat. Geosci.*, 2022, **15**, 967–975.
19 M. Ganguly and P. A. Ariya, *ACS Earth Space Chem.*, 2019, **3**, 1729–1739.
20 L. E. Revell, P. Kuma, E. C. Le Ru, W. R. C. Somerville and S. Gaw, *Nature*, 2021, **598**, 462–467.
21 T. M. Seifried, S. Nikkho, A. Morales Murillo, L. J. Andrew, E. R. Grant and A. K. Bertram, *Environ. Sci. Technol.*, 2024, **58**, 15711–15721.
22 Y. Wang, H. Okochi, Y. Tani, H. Hayami, Y. Minami, N. Katsumi, M. Takeuchi, A. Sorimachi, Y. Fujii, M. Kajino, K. Adachi, Y. Ishihara, Y. Iwamoto and Y. Niida, *Environ. Chem. Lett.*, 2023, **21**, 3055–3062.
23 S. B. Borrelle, J. Ringma, K. L. Law, C. C. Monnahan, L. Lebreton, A. McGivern, E. Murphy, J. Jambeck, G. H. Leonard, M. A. Hilleary, M. Eriksen, H. P. Possingham, H. De Frond, L. R. Gerber, B. Polidoro, A. Tahir, M. Bernard, N. Mallos, M. Barnes and C. M. Rochman, *Science*, 2020, **369**, 1515–1518.
24 M. Haward, *Nat. Commun.*, 2018, **9**, 667.
25 A. Stubbins, K. L. Law, S. E. Muñoz, T. S. Bianchi and L. Zhu, *Science*, 2021, **373**, 51–55.
26 I. Batool, A. Qadir, J. M. Levermore and F. J. Kelly, *Sci. Total Environ.*, 2022, **806**, 150745.
27 B. Gewert, M. M. Plassmann and M. MacLeod, *Environ. Sci.: Processes Impacts*, 2015, **17**, 1513–1521.
28 J. M. Sipe, N. Bossa, W. Berger, N. von Windheim, K. Gall and M. R. Wiesner, *Sci. Total Environ.*, 2022, **814**, 152460.
29 D. Allen, S. Allen, S. Abbasi, A. Baker, M. Bergmann, J. Brahney, T. Butler, R. A. Duce, S. Eckhardt, N. Evangeliou, T. Jickells, M. Kanakidou, P. Kershaw, P. Laj, J. Levermore, D. Li, P. Liss, K. Liu, N. Mahowald, P. Masque, D. Materić, A. G. Mayes, P. McGinnity, I. Osvath, K. A. Prather, J. M. Prospero, L. E. Revell, S. G. Sander, W. J. Shim, J. Slade, A. Stein, O. Tarasova and S. Wright, *Nat. Rev. Earth Environ.*, 2022, **3**, 393–405.
30 N. B. Hartmann, T. Hüffer, R. C. Thompson, M. Hassellöv, A. Verschoor, A. E. Daugaard, S. Rist, T. Karlsson, N. Brennholt, M. Cole, M. P. Herrling, M. C. Hess, N. P. Ivleva, A. L. Lusher and M. Wagner, *Environ. Sci. Technol.*, 2019, **53**, 1039–1047.
31 D. M. Mitrano, P. Wick and B. Nowack, *Nat. Nanotechnol.*, 2021, **16**, 491–500.
32 L. M. Hernandez, N. Yousefi and N. Tufenkji, *Environ. Sci. Technol. Lett.*, 2017, **4**, 280–285.
33 D. M. Mitrano and W. Wohlleben, *Nat. Commun.*, 2020, **11**, 5324.
34 J. Brahney, N. Mahowald, M. Prank, G. Cornwell, Z. Klimont, H. Matsui and K. A. Prather, *Proc. Natl. Acad. Sci. U. S. A.*, 2021, **118**, e2020719118.
35 S. Allen, D. Allen, S. Karbalaei, V. Maselli and T. R. Walker, *J. Hazard. Mater. Adv.*, 2022, **6**, 100057.
36 N. Evangeliou, H. Grythe, Z. Klimont, C. Heyes, S. Eckhardt, S. Lopez-Aparicio and A. Stohl, *Nat. Commun.*, 2020, **11**, 3381.
37 A. S. Keller, J. Jimenez-Martinez and D. M. Mitrano, *Environ. Sci. Technol.*, 2020, **54**, 911–920.
38 E. Marti, V. Osorio, M. Llorca, L. Paredes and M. Gros, *Advances in Chemical Pollution, Environmental Management and Protection*, Elsevier, 2020, vol. 6, pp. 137–180.
39 P. He, L. Chen, L. Shao, H. Zhang and F. Lü, *Water Res.*, 2019, **159**, 38–45.
40 M. Rezaei, M. J. Riksen, E. Sirjani, A. Sameni and V. Geissen, *Sci. Total Environ.*, 2019, **669**, 273–281.
41 K. J. Kapp and R. Z. Miller, *PLoS One*, 2020, **15**, e0239165.
42 T. Mehmood and L. Peng, *J. Hazard. Mater.*, 2022, **429**, 128391.
43 A. C. Morales, J. M. Tomlin, C. P. West, F. A. Rivera-Adorno, B. N. Peterson, S. A. L. Sharpe, Y. Noh, S. M. T. Sendesi, B. E. Boor, J. A. Howarter, R. C. Moffet, S. China, B. T. O'Callahan, P. Z. El-Khoury, A. J. Whelton and A. Laskin, *Nat. Nanotechnol.*, 2022, **17**, 1171–1177.
44 J. D. Drummond, U. Schneidewind, A. Li, T. J. Hoellein, S. Krause and A. I. Packman, *Sci. Adv.*, 2022, **8**, eabi9305.
45 L. Ferrero, L. Scibetta, P. Markuszewski, M. Mazurkiewicz, V. Drozdowska, P. Makuch, P. Jutrzenka-Trzebiatowska, A. Zaleska-Medynska, S. Andò, F. Saliu, E. D. Nilsson and E. Bolzacchini, *Sci. Total Environ.*, 2022, **824**, 153709.
46 A. Kelly, D. Lannuzel, T. Rodemann, K. M. Meiners and H. J. Auman, *Mar. Pollut. Bull.*, 2020, **154**, 111130.
47 K. Pabortsava and R. S. Lampitt, *Nat. Commun.*, 2020, **11**, 4073.
48 S. Allen, D. Allen, K. Moss, G. Le Roux, V. R. Phoenix and J. E. Sonke, *PLoS One*, 2020, **15**, e0232746.
49 M. Masry, S. Rossignol, B. Temime Roussel, D. Bourgogne, P. Bussière, B. R'mili and P. Wong-Wah-Chung, *Environ. Pollut.*, 2021, **280**, 116949.
50 M. Lehmann, L. M. Oehlschlägel, F. P. Häusl, A. Held and S. Gekle, *Microplast. Nanoplast.*, 2021, **1**, 18.
51 J. Brahney, M. Hallerud, E. Heim, M. Hahnenberger and S. Sukumaran, *Science*, 2020, **368**, 1257–1260.
52 Z. A. Kanji, L. A. Ladino, H. Wex, Y. Boose, M. Burkert-Kohn, D. J. Cziczo and M. Krämer, *Meteorol. Monogr.*, 2017, **58**, 1.1–1.33.

53 S. Mertes, B. Verheggen, S. Walter, P. Connolly, M. Ebert, J. Schneider, K. N. Bower, J. Cozic, S. Weinbruch, U. Baltensperger and E. Weingartner, *Aerosol Sci. Technol.*, 2007, **41**, 848–864.
54 D. Materić, E. Ludewig, D. Brunner, T. Röckmann and R. Holzinger, *Environ. Pollut.*, 2021, **288**, 117697.
55 D. Materić, H. A. Kjær, P. Vallelonga, J. Tison, T. Röckmann and R. Holzinger, *Environ. Res.*, 2022, **208**, 112741.
56 E. M. Esders, S. Sittl, I. Krammel, W. Babel, G. Papastavrou and C. K. Thomas, *Is Transport of Microplastics Different from that of Mineral Dust? Results from Idealized Wind Tunnel Studies*, Aerosols/laboratory studies/troposphere/physics (physical properties and processes) preprint, 2023.
57 S. Allen, D. Allen, F. Baladima, V. R. Phoenix, J. L. Thomas, G. Le Roux and J. E. Sonke, *Nat. Commun.*, 2021, **12**, 7242.
58 M. González-Pleiter, C. Edo, A. Aguilera, D. Viúdez-Moreiras, G. Pulido-Reyes, E. González-Toril, S. Osuna, G. de Diego-Castilla, F. Leganés, F. Fernández-Piñas and R. Rosal, *Sci. Total Environ.*, 2021, **761**, 143213.
59 Q. Chen, G. Shi, L. E. Revell, J. Zhang, C. Zuo, D. Wang, E. C. Le Ru, G. Wu and D. M. Mitrano, *Nat. Commun.*, 2023, **14**, 7898.
60 A. Azari, J. A. J. Vanoirbeek, F. Van Belleghem, B. Vleeschouwers, P. H. M. Hoet and M. Ghosh, *Environ. Int.*, 2023, **174**, 107885.
61 L. dos Santos Galvão, E. M. S. Fernandes, R. R. Ferreira, D. dos Santos Rosa and H. Wiebeck, *J. Hazard. Mater.*, 2022, **424**, 127668.
62 X. Luo, Z. Wang, L. Yang, T. Gao and Y. Zhang, *Sci. Total Environ.*, 2022, **828**, 154487.
63 S. Allen, D. Materić, D. Allen, A. MacDonald, R. Holzinger, G. L. Roux and V. R. Phoenix, *J. Hazard. Mater. Adv.*, 2022, **7**, 100104.
64 S. Niu, R. Liu, Q. Zhao, S. Gagan, A. Dodero, Q. Ying, X. Ma, Z. Cheng, S. China, M. Canagaratna and Y. Zhang, *Environ. Sci. Technol.*, 2024, 3363–3374.
65 T. Menzel, N. Meides, A. Mauel, U. Mansfeld, W. Kretschmer, M. Kuhn, E. M. Herzig, V. Altstädt, P. Strohriegl, J. Senker and H. Ruckdäschel, *Sci. Total Environ.*, 2022, **826**, 154035.
66 U. Lohmann, F. Luond and F. Mahrt, *An Introduction to Clouds: from the Microscale to Climate*, Cambridge University Press, Cambridge, 2016.
67 H. R. Pruppacher and J. D. Klett, *Microphysics of Clouds and Precipitation*, Springer Netherlands, 2010, vol. 18.
68 L. Cai, J. Wang, J. Peng, Z. Tan, Z. Zhan, X. Tan and Q. Chen, *Environ. Sci. Pollut. Res.*, 2017, **24**, 24928–24935.
69 R. B. Schefer, A. Armanious and D. M. Mitrano, *Environ. Sci. Technol.*, 2023, **57**, 14707–14716.
70 C. Marcolli, *Atmos. Chem. Phys.*, 2014, **14**, 2071–2104.
71 D. M. Mitrano, A. Beltzung, S. Frehland, M. Schmiedgruber, A. Cingolani and F. Schmidt, *Nat. Nanotechnol.*, 2019, **14**, 362–368.
72 Y. Zhang, S. Kang, S. Allen, D. Allen, T. Gao and M. Sillanpää, *Earth-Sci. Rev.*, 2020, **203**, 103118.
73 Z. A. Kanji and J. P. D. Abbatt, *Aerosol Sci. Technol.*, 2009, **43**, 730–738.
74 L. Lacher, U. Lohmann, Y. Boose, A. Zipori, E. Herrmann, N. Bukowiecki, M. Steinbacher and Z. A. Kanji, *Atmos. Chem. Phys.*, 2017, **17**, 15199–15224.
75 D. Lamb and J. Verlinde, *Physics and Chemistry of Clouds*, Cambridge University Press, Cambridge, 2011.
76 R. R. Rogers and M. K. Yau, *A Short Course in Cloud Physics*, Pergamon Press, 1989, vol. 113.
77 A. Wiedensohler, *J. Aerosol Sci.*, 1988, **19**, 387–389.
78 A. Alshawa, O. Dopfer, C. W. Harmon, S. A. Nizkorodov and J. S. Underwood, *J. Phys. Chem. A*, 2009, **113**, 7678–7686.
79 A. Bain and T. C. Preston, *Environ. Sci. Technol.*, 2021, **55**, 11775–11783.
80 D. Ferry, J. Suzanne, S. Nitsche, O. B. Popovitcheva and N. K. Shonija, *J. Geophys. Res.: Atmos.*, 2002, **107**, AAC 22-1–AAC 22-10.
81 M. Thommes, K. Kaneko, A. V. Neimark, J. P. Olivier, F. Rodriguez-Reinoso, J. Rouquerol and K. S. W. Sing, *Pure Appl. Chem.*, 2015, **87**, 1051–1069.
82 D. M. Murphy and T. Koop, *Q. J. R. Metereol. Soc.*, 2005, **131**, 1539–1565.
83 K. Gao and Z. A. Kanji, *Geophys. Res. Lett.*, 2024, **51**, e2023GL106926.
84 R. O. David, C. Marcolli, J. Fahrni, Y. Qiu, Y. A. Perez Sirkin, V. Molinero, F. Mahrt, D. Brühwiler, U. Lohmann and Z. A. Kanji, *Atmos. Chem. Phys.*, 2019, **116**, 8184–8189.
85 C. Marcolli, F. Mahrt and B. Kärcher, *Atmos. Chem. Phys.*, 2021, **21**, 7791–7843.
86 M. Lbadaoui-Darvas, A. Laaksonen and A. Nenes, *Atmos. Chem. Phys.*, 2023, **23**, 10057–10074.
87 W. He, S. Liu, W. Zhang, K. Yi, C. Zhang, H. Pang, D. Huang, J. Huang and X. Li, *Sci. Total Environ.*, 2023, **889**, 164035.
88 K. Li, Y. Guo, S. A. Nizkorodov, Y. Rudich, M. Angelaki, X. Wang, T. An, S. Perrier and C. George, *Proc. Natl. Acad. Sci. U. S. A.*, 2023, **120**, e2220228120.
89 W. Mei, G. Chen, J. Bao, M. Song, Y. Li and C. Luo, *Sci. Total Environ.*, 2020, **736**, 139472.
90 N. Qian, X. Gao, X. Lang, H. Deng, T. M. Bratu, Q. Chen, P. Stapleton, B. Yan and W. Min, *Proc. Natl. Acad. Sci. U. S. A.*, 2024, **121**, e2300582121.
91 A. Kumar, C. Marcolli and T. Peter, *Atmos. Chem. Phys.*, 2019, **19**, 6059–6084.
92 A. Kumar, A. K. Bertram and G. N. Patey, *ACS Earth Space Chem.*, 2021, **5**, 2169–2183.
93 R. C. Sullivan, L. Miñambres, P. J. DeMott, A. J. Prenni, C. M. Carrico, E. J. T. Levin and S. M. Kreidenweis, *Geophys. Res. Lett.*, 2010, **37**, 2010GL045540.
94 R. C. Sullivan, M. D. Petters, P. J. DeMott, S. M. Kreidenweis, H. Wex, D. Niedermeier, S. Hartmann, T. Clauss, F. Stratmann, P. Reitz, J. Schneider and B. Sierau, *Atmos. Chem. Phys.*, 2010, **10**, 11471–11487.
95 K. Gao, F. Friebel, C. Zhou and Z. A. Kanji, *Atmos. Chem. Phys.*, 2022, **22**, 4985–5016.
96 K. Gao, C. Zhou, E. J. Barthazy Meier and Z. A. Kanji, *Atmos. Chem. Phys.*, 2022, **22**, 5331–5364.
97 A. Welti, F. Lüönd, O. Stetzer and U. Lohmann, *Atmos. Chem. Phys.*, 2009, **9**, 6705–6715.

98 P. J. DeMott, D. J. Cziczo, A. J. Prenni, D. M. Murphy, S. M. Kreidenweis, D. S. Thomson, R. Borys and D. C. Rogers, *Proc. Natl. Acad. Sci. U. S. A.*, 2003, **100**, 14655–14660.
99 M. Bergmann, S. Mützel, S. Primpke, M. B. Tekman, J. Trachsel and G. Gerdts, *Sci. Adv.*, 2019, **5**, eaax1157.
100 P. K. Lindeque, M. Cole, R. L. Coppock, C. N. Lewis, R. Z. Miller, A. J. Watts, A. Wilson-McNeal, S. L. Wright and T. S. Galloway, *Environ. Pollut.*, 2020, **265**, 114721.